Finite Element and Experimental Studies on the Machining Process of Polymer/Graphene Nanoplatelet Nanocomposites

Guoyu Fu[1], Fuzhong Sun[2],Fengzhen Sun[3], Dehong Huo[1*], Islam Shyha[4], Chenggang Fang[2], Qiang Gao[5]

[1.] *School of Engineering, Newcastle University, Newcastle upon Tyne, NE1 7RU, UK.*
[2.] *School of Mechanical and Power Engineering, Nanjing Tech University, Nanjing, Jiangsu 211816, China*
[3.] *Department of Mechanical Engineering, Imperial College London, London SW7 2AZ, UK.*
[4.] *School of Engineering and the Built Environment, Edinburgh Napier University, Edinburgh EH10 5DT, UK*
[5.] *School of Mechatronics Engineering, Harbin Institute of Technology, PO Box 413, 92 West Dazhi Street, Nan Gang District, Harbin 150001, China*

*Corresponding author: D. Huo, Tel.: +44 (0)1912086230, *E-mail address:* dehong.huo@newcastle.ac.uk

Abstract

Polymer matrix composites reinforced with graphene derivatives are receiving increasing attention in academia and industry. For future applications, however, the machinability of these materials needs to be understood. This study introduces the cutting mechanism of graphene nanoplatelet (GNP)-reinforced polymer matrix composites using the finite element (FE) method, where the cutting process is investigated in terms of stress distribution, chip formation, and surface morphology. The results show that the machined surface of polymer/GNP material has more defects compared with plain polymer and the presence of the GNPs influences the chip profiles. Small cavities/cracks can be found in about 40% area of machined surface in the epoxy/GNP, while no small cavities/cracks are found on the machined surface of plain epoxy. The machining conditions of epoxy/GNP should be selected in such a way that the material removal deformation falls in the regime without viscoplastic scaling/tearing and brittle cracking. The cutting model for polymer/GNP is validated with the machining experiments.

Keyword: Finite element (FE), Polymer/graphene nanoplatelet (GNP) nanocomposites, Machining

1 Introduction

Polymer/nanoparticle nanocomposites have received extensive attention in industry due to their outstanding properties. Nanoparticles can be defined in terms of the design, synthesis, characterisation, and application of materials. The smallest functional organisation of these particles has at least one dimension in the order of nanometres or billionths of one metre [1]. The nanostructure of the particles provides opportunities for the development of new materials

[2-4], and research has shown that adding small amounts of nanoparticles can improve the electrical, mechanical and thermal properties of a polymer matrix [5-10].

Graphene is an atomically thick, two-dimensional (2-D) layer composed of sp^2 carbon atoms arranged in a honeycomb structure [11]. It has excellent mechanical properties, including a high Young's modulus of 1,000 GPa, high fracture strength of 125 GPa, high thermal conductivity of 5,000 $Wm^{-1}K^{-1}$, and a charge carrier mobility of 200,000 $cm^2V^{-1}s^{-1}$ [12]. Due to such superior features, the applications of graphene materials have attracted great interest. Graphene nanoplatelets (GNPs) have gradually come to be regarded as ideal nanoparticles for improving the mechanical properties of matrix materials [13], since GNP nanoparticles are more efficient compared with other nanoparticles derived from graphene. This is because GNP has a larger surface area and can enhance interfacial interaction [14-18]. Atif et al. [19] showed that the addition of 0.1 wt% GNPs can lead to increases of Young's modulus by 26% and flexural moduli by 23% compared with the plain polymer. Rafiee et al. [11] found that significant increase (up to 52%) in critical buckling load is observed with addition of only the addition of 0.1 wt % GNP into the epoxy matrix. The GNP nanoparticles can increase the flexural modulus of the matrix without losing the flexural strength, apart from improving the fracture toughness and impact energy [13,20]. Overall, the addition of GNP nanoparticles generally improves matrix materials and changes their properties/functions [11], and in most cases the addition of GNPs is reported at amounts below 1.0 wt%.

Polymer/GNP nanocomposites have a wide range of applications in the electronics industry, including as material for electrodes [21] and capacitors [22]. Electronics products have high surface and dimensional accuracy as well as small features such as micro-holes. Therefore, the machinability of electronic material is crucial. Samuel et al. [23] studied the micro machining of polymer nanocomposites in terms of cutting forces, tool wear, surface roughness, and chip morphology. The nanocomposite and the carbon fibre composite are seen to have the lowest and the highest magnitudes, respectively, for both the surface roughness and cutting forces. Shearing along the nanotube-polymer interface and better thermal conductivity are speculated to be the mechanisms responsible for the observations seen in the nanocomposite.

However, research on the machinability of polymer/GNP nanocomposites is still very limited and the effect of GNP nanoparticles on machining processes during manufacture is not yet well understood. To bridge this gap, the finite element (FE) method was used in this study to investigate the machinability of polymer/GNP nanocomposites. This method provides a tool to explore the mechanisms involved in the removal of nanocomposite material [24] and can be used to predict nanoparticle behaviour such as in debonding and fracture which occurs during the cutting process.

In this paper, a novel FE model for machining GNP nanoparticle-reinforced polymers is developed. The paper is organized as follows: Sections 2 and 3 describe the preparation of the workpiece material and the experimental procedure respectively; section 4 presents the models used for the polymer material and the FE cutting process; section 5 reports the results along with a discussion of the stress/strain distribution, tool-particle interaction and surface morphology after the machining of the polymer/GNP nanocomposites and plain polymer; Section 6 summarizes the conclusions drawn from this study.

2 Preparation of Polymer/GNP Nanocomposite Material

The GNP nanoparticles were dispersed in the hardener by bath sonication at room temperature for 30 minutes, after which a suspension containing GNP nanoparticles was obtained. The suspension and the liquid polymer resin were then combined and mixed at a resin ratio of 2:1 for 10 minutes. The mixed liquid was hardened and degassed in vacuum conditions to remove entrained air before being shaped and cured at room temperature for 6 hours and then at 80 °C for 6 hours [7]. The polymer material used in this study is epoxy, and **Figs. 1** and **2** show scanning electron microscopy (SEM) images of the epoxy/GNP 0.1 wt% nanocomposite and plain epoxy used in this study respectively. **Fig. 2 (a)** shows a single GNP distributed in the epoxy matrix and **Fig. 2 (b)** presents GNP clusters in the epoxy. **Fig. 2 (c)** illustrates the fracture surfaces of plain epoxy, where river-like markings indicate the typical brittle fracture observed in this material [25]**. Fig. 2 (d)** shows the fracture surfaces of epoxy/GNP 0.1wt% nanocomposites [26]. The epoxy/GNP nanocomposite has a rough pit-like fracture surface, indicating a change in fracture mode from brittle to ductile fracture [27].

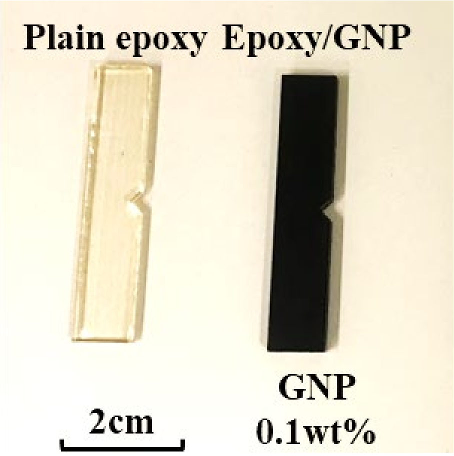

Figure 1. Epoxy/GNP nanocomposites and plain epoxy samples for micro-milling experiments

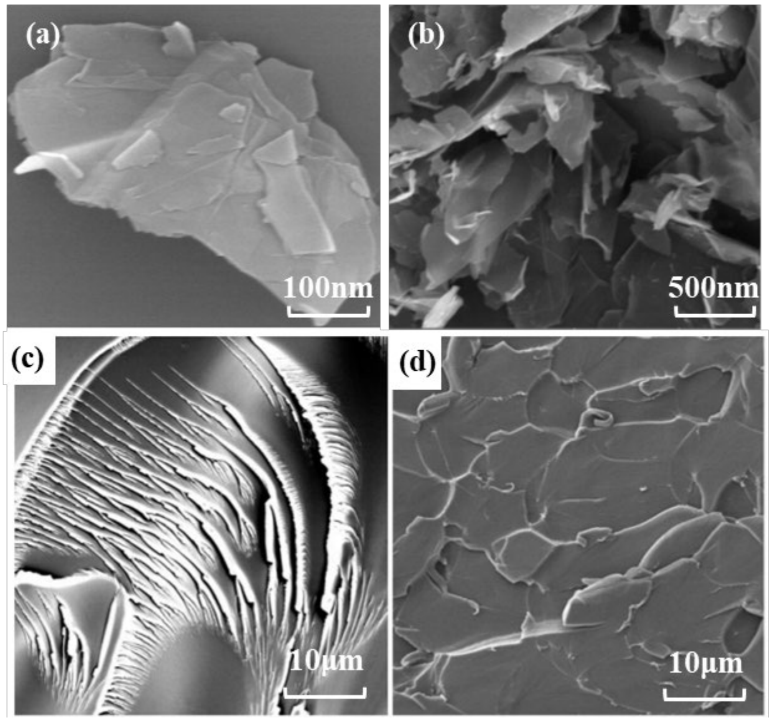

Figure 2. Scanning electron microscopy (SEM) images of: (a) single GNP in matrix material, reproduced from [26]; (b) GNP clusters in matrix material, reproduced from [28]; (c) fracture surfaces of plain epoxy, reproduced from [26]; and (d) fracture surfaces of epoxy/GNP 0.1 wt%, reproduced from [26]

3 Experimental Validation

Micromachining of the epoxy/GNPs nanocomposites was carried out in order to verify the FE modelling result including the characteristics of chip deformation and the machined surface. The experimental process was conducted in dry conditions on an ultra-precision desktop micromachine (MTS5R), as shown in **Fig. 3**. It has a continuous power of 100 W (240 V) and a maximum spindle speed of 80,000 rpm controlled by a DC servo motor that consists of 3 axes (X, Y, Z), with a move accuracy of 0.1 μm. **Fig. 4** shows the schematics of a machined slot and the relationship between a simplified 2D micro-milling process and the orthogonal cutting process. The maximum chip thickness of about 1.0 μm is much smaller than the tool diameter of 1000 μm. Compared with the travel distance of the cutting edge at a rotation angle of 180° (about 392.5 μm), the change in chip thickness of 1 μm is relatively small. It is assumed that the 3D micro-milling process can be simplified into a 2D micro-orthogonal machining process. **Tables 1** and **2** respectively list the micro-end milling specifications and machining parameters used in this study. The cutting in the experiment has two levels of cutting speed (62.8 and 251.2 m/min) and two levels of feed per tooth (FPT) (2.0 and 5.0 μm/tooth).

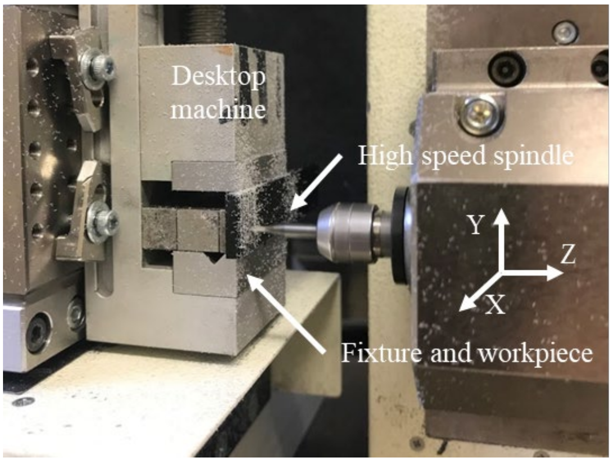

Figure 3. The micro-milling process of epoxy/GNP nanocomposites on an ultra-precision desktop

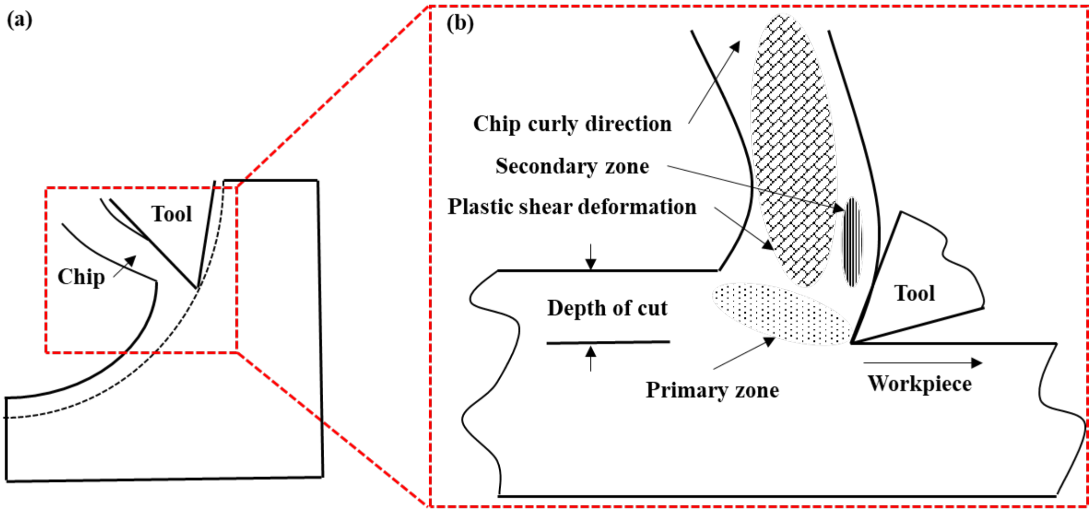

Figure 4. The milling process: (a) schematic diagram of 2D milling; and (b) relationship between the 2D milling and orthogonal machining processes, reproduced from [29]

Table 1. Micro-end milling uncoated tool specifications

Properties	Value
Tool diameter	1.0 mm
Number of flutes	2
Flute style	Right-hand spiral/medium helix
Finish/coating	Uncoated
Helix angle	30°
Tool edge radius	1.5 μm

Table 2. Cutting conditions for the experiment and FE process

Cutting speed (m/min)	Feed per tooth (μm/tooth)	Depth of cut (mm)
62.8, 251.2	2.0, 5.0	0.1

4 Material Constitutive Model and FE Cutting Model

4.1 Mulliken-Boyce Constitutive Model for Polymer

Polymers are ductile at room temperature and fracture in the same way as ductile metal materials. The difference in ductile fracturing between metals and polymers involves the matrix material surrounding impurities and voids. Therefore, a constitutive material model of polymer materials should be developed to describe the effect of polymer geometry on the material's properties at a microscopic scale. Several such models have been built for polymer material, such as the Arruda-Boyce model [30], Mulliken-Boyce model [31,32] among others. These constitutive models for polymers have not yet been established in commercial FE software. Thus, user-defined material subroutines were used to build constitutive models for commercial FE software. The Mulliken-Boyce model was chosen in this study and was implemented using VUMAT. The selection of this model was mainly because it can capture the mechanical behaviour at intermediate to high strain rates.

The Mulliken-Boyce model is a physics-based constitutive model based on the theory of large plasticity, which characterises the elasticity, yield and post-yield behaviour of polymers from low to high strain rates [31,33]. Due to the large deformation of the polymer, two physical resistances need to be overcome before large inelastic flow occurs. When the material flows freely, orientation hardening occurs. Directional hardening is a molecular arrangement that causes further inelastic deformation of anisotropic internal resistance, as shown in **Fig. 5**. The Mulliken-Boyce model includes two activated molecular processes. Each has its own definition of elasticity and viscoplasticity which are parallel to each other and parallel to the nonlinear entropy hardening component [31,33]. The one-dimensional rheological description of the proposed constitutive model is shown in **Fig. 6**. This model provides an in-depth explanation of the molecular mechanism that hinders high-speed deformation. The proposed model's basic principles closely resemble Ree-Eyring yield theory based on many activation processes. These activation processes represent motions at various molecular levels. Each process has a threshold determined by temperature and deformation rate. Below this, the related molecular movement is restricted. When the action is limited, the overall resistance to deformation of the material is improved.

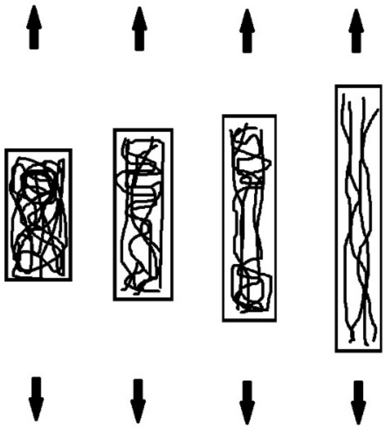

Figure 5. Rotation of the molecules of polymer material during deformation

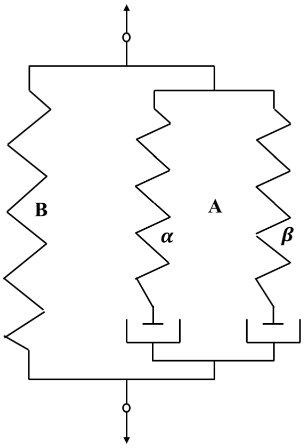

Figure 6. One-dimensional rheological interpretation of the proposed constitutive model, reproduced from [33]

4.2 Mullikin-Boyce Model Kinematics

In the Mulliken–Boyce model [31], the kinematic analysis begins with the deformation gradient, *F*, which maps a material point from its reference position *X* to the current location *x*:

$$F \equiv \frac{x}{X} \tag{1}$$

Upon loading, all components experience the same deformation:

$$F \equiv F_{A_\alpha} = F_{A_\beta} = F_B \tag{2}$$

The deformation gradient in elements *α* and *β* are multiplicatively decomposed into elastic and plastic components via Kroner-Lee decomposition:

$$F_{A_\alpha} = F^e_{A_\alpha} F^p_{A_\alpha} \tag{3}$$

$$F_{A_\beta} = F^e_{A_\beta} F^p_{A_\beta} \tag{4}$$

Assuming that the plastic deformation is a volume-preserving process, then:

$$det\, F^p_{A_\alpha} = det\, F^p_{A_\beta} = 1 \tag{5}$$

All volume-changing deformation is elastic:

$$det\, F^e_{A_\alpha} = det\, F^e_{A_\beta} = J \tag{6}$$

Therefore the deformation of the relaxed configuration can be expressed as:

$$F^p_{A_\alpha} = \mathrm{R}^p_{A_\alpha} U^p_{A_\alpha} = V^p_{A_\alpha} U^p_{A_\alpha} \tag{7}$$

$$F^p_{A_\beta} = \mathrm{R}^p_{A_\beta} U^p_{A_\beta} = V^p_{A_\beta} U^p_{A_\beta} \tag{8}$$

The velocity gradients in terms of the elastic and plastic components are shown as follows:

$$L_{A_\alpha} = L^p_{A_\alpha} + F^e_{A_\alpha} L^p_{A_\alpha} F^{e-1}_{A_\alpha} \tag{9}$$

and

$$L_{A_\beta} = L^p_{A_\beta} + F^e_{A_\beta} L^p_{A_\beta} F^{e-1}_{A_\beta} \tag{10}$$

where:

$$L_{A_\alpha}^{p} = \dot{F}_{A_\alpha}^{p} F_{A_\alpha}^{p-1} = D_{A_\alpha}^{p} + W_{A_\alpha}^{p} \tag{11}$$

$$L_{A_\beta}^{p} = \dot{F}_{A_\beta}^{p} F_{A_\beta}^{p-1} = D_{A_\beta}^{p} + W_{A_\beta}^{p} \tag{12}$$

The next step is that plastic flow is irrotational in both the α and β components:

$$W_{A_\alpha}^{p} + W_{A_\beta}^{p} = 0 \tag{13}$$

and therefore:

$$\dot{F}_{A_\alpha}^{p} = D_{A_\alpha}^{p} F_{A_\alpha}^{p} \tag{14}$$

$$\dot{F}_{A_\beta}^{p} = D_{A_\beta}^{p} F_{A_\beta}^{p} \tag{15}$$

Equations 14 and **15** are integrated to obtain $F_{A_\alpha}^{p}$ and $F_{A_\beta}^{p}$, and the elastic deformation gradients are then obtained via:

$$F_{A_\alpha}^{e} = F_{A_\alpha} F_{A_\alpha}^{p-1} \tag{16}$$

$$F_{A_\beta}^{e} = F_{A_\beta} F_{A_\beta}^{p-1} \tag{17}$$

Finally, the plastic flow rules are given by:

$$D_{A_\alpha}^{p} = \dot{\gamma}_{A_\alpha}^{p} N_{A_\alpha}^{p} \tag{18}$$

$$D_{A_\beta}^{p} = \dot{\gamma}_{A_\beta}^{p} N_{A_\beta}^{p} \tag{19}$$

where:

$$N_{A_\alpha}^{p} = \frac{T_{A_\alpha}^{'}}{\left|T_{A_\alpha}^{'}\right|} \tag{20}$$

$$N_{A_\beta}^{p} = \frac{T_{A_\beta}^{'}}{\left|T_{A_\beta}^{'}\right|} \tag{21}$$

4.3 Mullikin-Boyce Model Material Description and Constitutive Relations

As with the original structure of the model, the intermolecular contribution to the material stress state is related to the deformation according to the constitutive laws for linear elastic springs:

$$T_{A_\alpha} = \frac{1}{J_\alpha}\mathscr{L}^e_\alpha\left[InU^e_{A_\alpha}\right] \tag{22}$$

$$T_{A_\beta} = \frac{1}{J_\beta}\mathscr{L}^e_\beta\left[InU^e_{A_\beta}\right] \tag{23}$$

where $T_{A_i}(i = \alpha, \beta)$ is the Cauchy (true) stress, $\mathcal{L}^e_i$ is the fourth-order modulus tensor, and ln $U^e_{A_i}$is the Hencky strain. It is assumed that the material is initially isotropic and that the elastic behaviour of the material may be decomposed into α and β components. The modulus tensors may be derived from any two component-specific elastic constants, such as the shear modulus μ and bulk modulus κ:

$$\mathcal{L}^e_\alpha = 2\mu_\alpha\mathcal{J} + (\kappa_\alpha - \frac{2}{3}\mu_\alpha)I \otimes I \tag{24}$$

$$\mathcal{L}^e_\beta = 2\mu_\beta\mathcal{J} + (\kappa_\beta - \frac{2}{3}\mu_\beta)I \otimes I \tag{25}$$

where $\mathcal{J}$ and I are the fourth-order and second-order identity tensors respectively. The elastic constants – in this case, μ_i and κ_i (i=α, β) – are assumed to be functions of both temperature and strain rate.

The stress in the nonlinear hardening component, which represents the network 'back stress' due to entropic resistance to molecular alignment, is defined precisely as before:

$$T_B = \frac{C_R}{3}\frac{\sqrt{N}}{\lambda^p_{chain}}\mathscr{L}^{-1}\left(\frac{\lambda^p_{chain}}{\sqrt{N}}\right)B_B^{'} \tag{26}$$

where λ^p_{chain} is the stretch on a chain in the eight-chain network; $\mathcal{L}$ is the Langevin function defined by $\mathscr{L}(\beta) \equiv coth\,\beta - \frac{1}{\beta}$; $B_B^{'}$ is the deviatoric part of the left Cauchy-Green tensor, $F_BF_B^T$; $\sqrt{N}$is the limiting chain extensibility; and $C_R \equiv nk\theta$ is the rubbery modulus.

The total stress in the polymer is given as the tensorial sum of the α and β intermolecular stresses and the network (back) stress:

$$T = T_{A_\alpha} + T_{A_\beta} + T_B \tag{27}$$

The driving stresses are used to specify the direction tensors $N^p_{A_\alpha}$and $N^p_{A_\beta}$in the plastic flow rules:

$$N_\alpha = \frac{1}{\sqrt{2}\tau_\alpha}T^{'}_{A_\alpha} \tag{28}$$

$$N_\beta = \frac{1}{\sqrt{2}\tau_\beta} T^{'}_{A_\beta} \tag{29}$$

The effective equivalent shear stresses τ_α and τ_β are given by:

$$\tau_\alpha = \sqrt{\frac{1}{2} T^{'}_{A_\alpha} T^{'}_{A_\alpha}} \tag{30}$$

$$\tau_\beta = \sqrt{\frac{1}{2} T^{'}_{A_\beta} T^{'}_{A_\beta}} \tag{31}$$

Varghese and Batra [34] modified the flow rule in the Mulliken–Boyce model [31] by including new internal variables to characterize the viscoplastic behaviour. Two constitutive laws are prescribed for α and β viscoplastic behaviour:

$$\dot{\gamma}^p_\alpha = \dot{\gamma}^p_{0,\alpha}\, exp\left[-\frac{\Delta G_\alpha}{k\theta}\left(1 - \frac{\tau_\alpha}{s_\alpha + \alpha_{\alpha+\beta} p}\right)\right] \tag{32}$$

$$\dot{\gamma}^p_\beta = \dot{\gamma}^p_{0,\beta}\, exp\left[-\frac{\Delta G_\beta}{k\theta}\left(1 - \frac{\tau_\alpha}{s_\beta + \alpha_{\alpha+\beta} p}\right)\right] \tag{33}$$

where $\dot{\gamma}^p_{0,i}$ $(i = \alpha, \beta)$ is the pre-exponential factor proportional to the attempt frequency,

ΔG_i is the activation energy, p is the pressure, and $\alpha_{p,i} p$ is the pressure coefficient. The internal variable s_i is the shear strength, which is related to the shear modulus and is said to evolve to a preferred state with plastic straining:

$$s_{0,\alpha} \equiv \frac{0.077\mu_\alpha}{1 - \nu_\alpha} \tag{34}$$

$$\dot{s}_\alpha = \hbar_\alpha \left(1 - \frac{s_\alpha}{s_{ss,a}}\right) \dot{\gamma}^p_\alpha \tag{35}$$

$$s_{0,\beta} \equiv \frac{0.077\mu_\beta}{1 - \nu_\beta} \tag{36}$$

$$\dot{s}_\beta = \hbar_\beta \left(1 - \frac{s_\beta}{s_{ss,\beta}}\right) \dot{\gamma}^p_\beta \tag{37}$$

where h_i $(i = \alpha, \beta)$ is the softening slope and $s_{ss,i}$ is the “preferred state”. This internal variable allows the temperature dependence of the yield stress to mimic the temperature dependence of the elastic shear moduli, and its evolution captures the strain-softening phenomenon. In the most general form of this constitutive model, the strain-softening phenomenon may be considered the sum of the softening in the α and β components. Furthermore, during the FEA processing, GNP nanoparticles are regarded as brittle fractures [35].

4.4 Mullikin-Boyce Model Parameters for Epoxy

Based on the one-dimensional version of the Mulliken-Boyce model, experimental data based on a genetic algorithm was used to analyse the constitutive parameters that drive the stress-strain behaviour of epoxy [36], as shown in **Table 3**. Here, the built-in Abaqus shear damage model was used, and the epoxy will degrade linearly after the equivalent strain has reached the critical value.

Table 3. Epoxy material parameters defined in the Mullikin-Boyce model [36]

Symbol	Unit	Value
$S_{ss,a}$	MPa	0.670
$\dot{\gamma}_{0,a}$	$10^{15}s^{-1}$	178
$\dot{\gamma}_{0,\beta}$	$10^{6}s^{-1}$	0.542
ΔG_{α}	$10^{-18}J$	0.967
ΔG_{β}	$10^{-21}J$	834
$\alpha_{p,\alpha}$		0.224
$\alpha_{p,\beta}$		0.378
h_{α}	MPa	263
C_R	MPa	13.9
N	$m^{-\frac{1}{2}}$	2.02
σ_{β}	MPa	0.283

4.5 FE Cutting Model

Fig. 7 shows the simplification strategy for the model of epoxy/GNP nanocomposites, where the FE model was simplified to 2-phase modelling. GNP nanoparticles are uniformly distributed in the matrix material model and are simplified to circles with a diameter of 500 nm. Simultaneously, a model of the same size without nanoparticles was also established as a control group. **Fig. 8** shows the FE model set-up for the FE model of the orthogonal cutting of epoxy/GNP. The cutting tool is regarded as an analytical rigid body which moves to a fixed workpiece at a certain speed. In the cutting model, the polymer matrix and GNP nanoparticle geometries are drawn separately. The geometries are assembled, and their interfaces are tied with no layer. The matrix and nanoparticles are meshed without sharing node. . The cutting conditions of the FE process are consistent with the experimental process.

There exists a wide range of variation in the properties of GNPs in the literature [37-41]. The density, Young's modulus, shear modulus, Poisson's ratio, critical stress intensity factor and equivalent critical strain energy release rate of GNP of this study are 2.267 g/cm^3 [37], 1 TPa [38], 280 GPa [38] , −0.38 [38], 4.0 MPa$\sqrt{m}$ [41], and 15.9 Jm^{-2} [41], respectively.

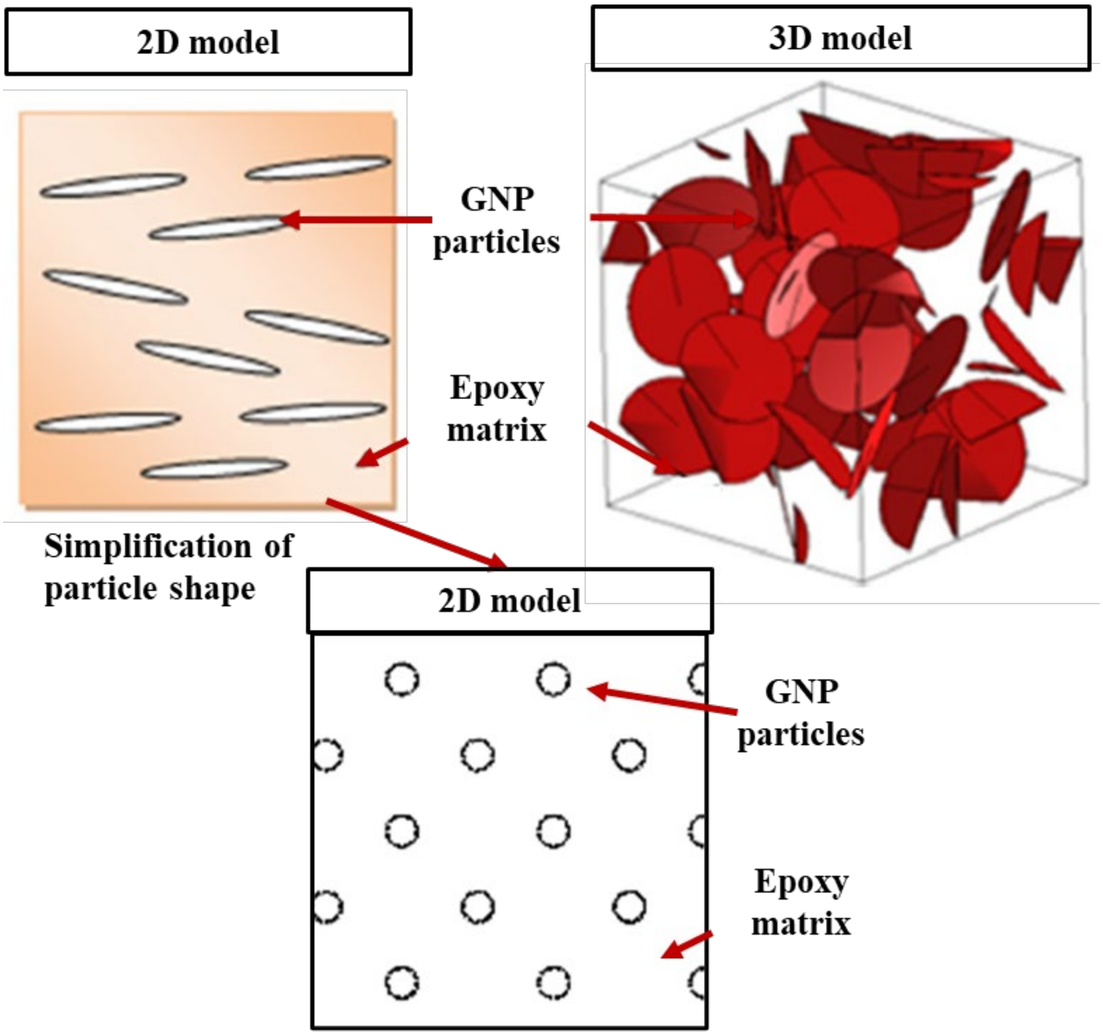

Figure 7. Simplification of the modelling of polymer/GNP nanocomposites, reproduced from [42]

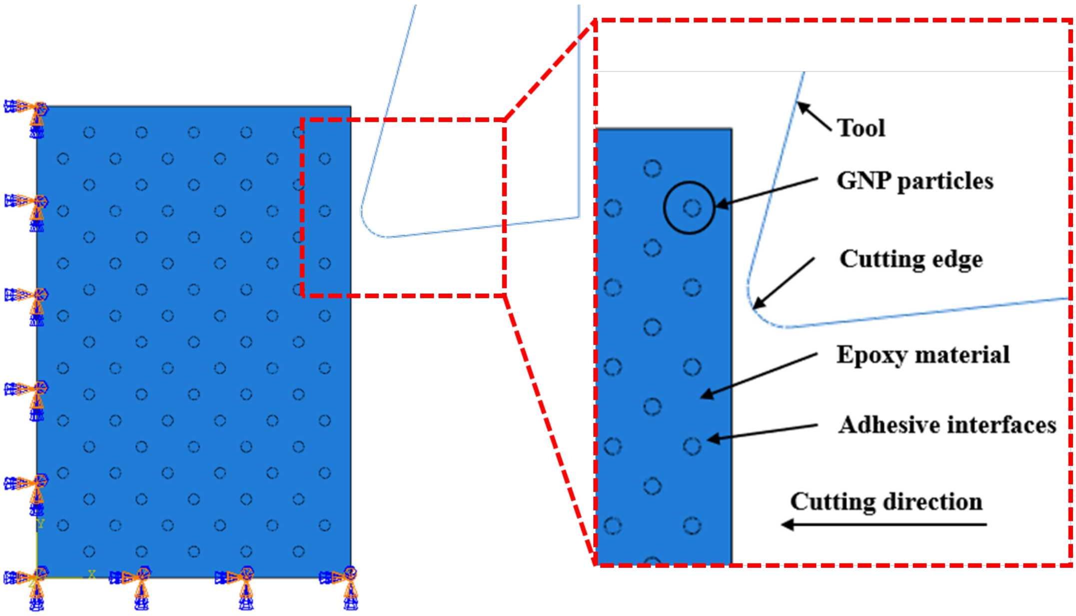

Figure 8. FE set-up for the orthogonal epoxy/GNP model

5. Results and Discussion

5.1. Stress Distribution

Fig. 9 shows the stress distribution when cutting plain epoxy and epoxy/GNP at 2 µm feed per tooth. Plain epoxy presents a highly concentrated stress area in the tool-workpiece contact area , while the contact area between the tool and the epoxy/GNP workpiece is associated with less stress concentration. . The GNP nanoparticles are subjected to high stress at the initial cutting stage, while the deformation in the matrix material intensifies gradually as the tool moves and more nanoparticles start to to high stress. This phenomenon indicates that GNP nanoparticles bear high stress transferred from the matrix material during the cutting process.

Fig. 10 presents the stress distribution in the plain epoxy and epoxy/GNP in the cutting condition of 5 µm feed per tooth. The difference in stress distribution between the plain epoxy and epoxy/GNP is more significant. The added GNP nanoparticles are found to act as barriers which resist the propagation of stress and divert highly concentrated stress to the surrounding area. With the tool's movement and the propagation of the shear plane, the stress tends to bypass the nanoparticles, which results in an irregular stress profile at each nanoparticle. Therefore, the GNP nanoparticles change the stress distribution during the cutting process so that the formation of shear zone is significantly confined. As a result, a different shear zone develops in the epoxy/GNP matrix material compared to that in the plain epoxy, and this ultimately affects the formation of the epoxy/GNP chip. The plain epoxy shows a serrated chip at the cutting speed of 251.2 m/min, whereas the epoxy/GNP shows continuous chips at this cutting speed. This phenomenon can be attributed to the change in the stress distribution caused by the GNP nanoparticles.

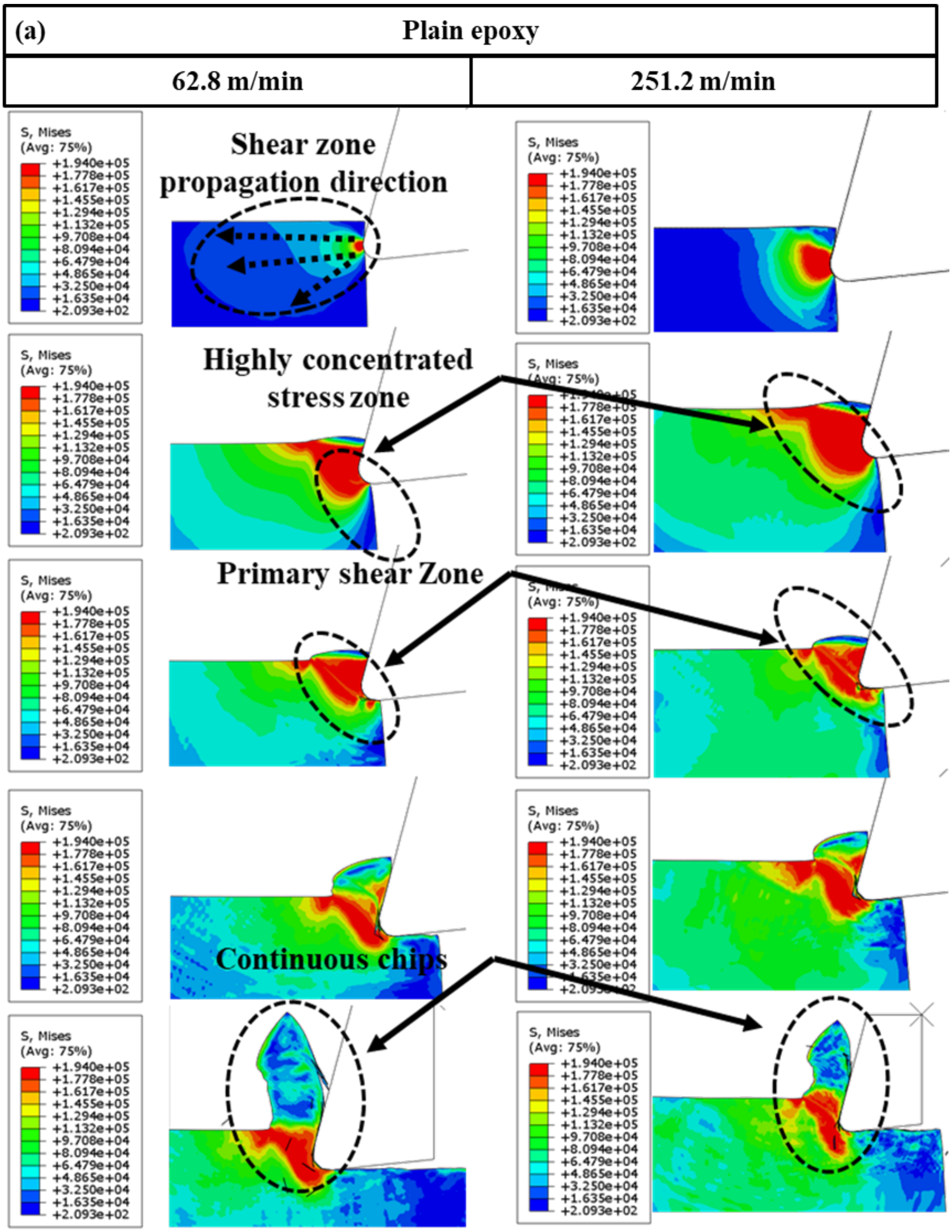

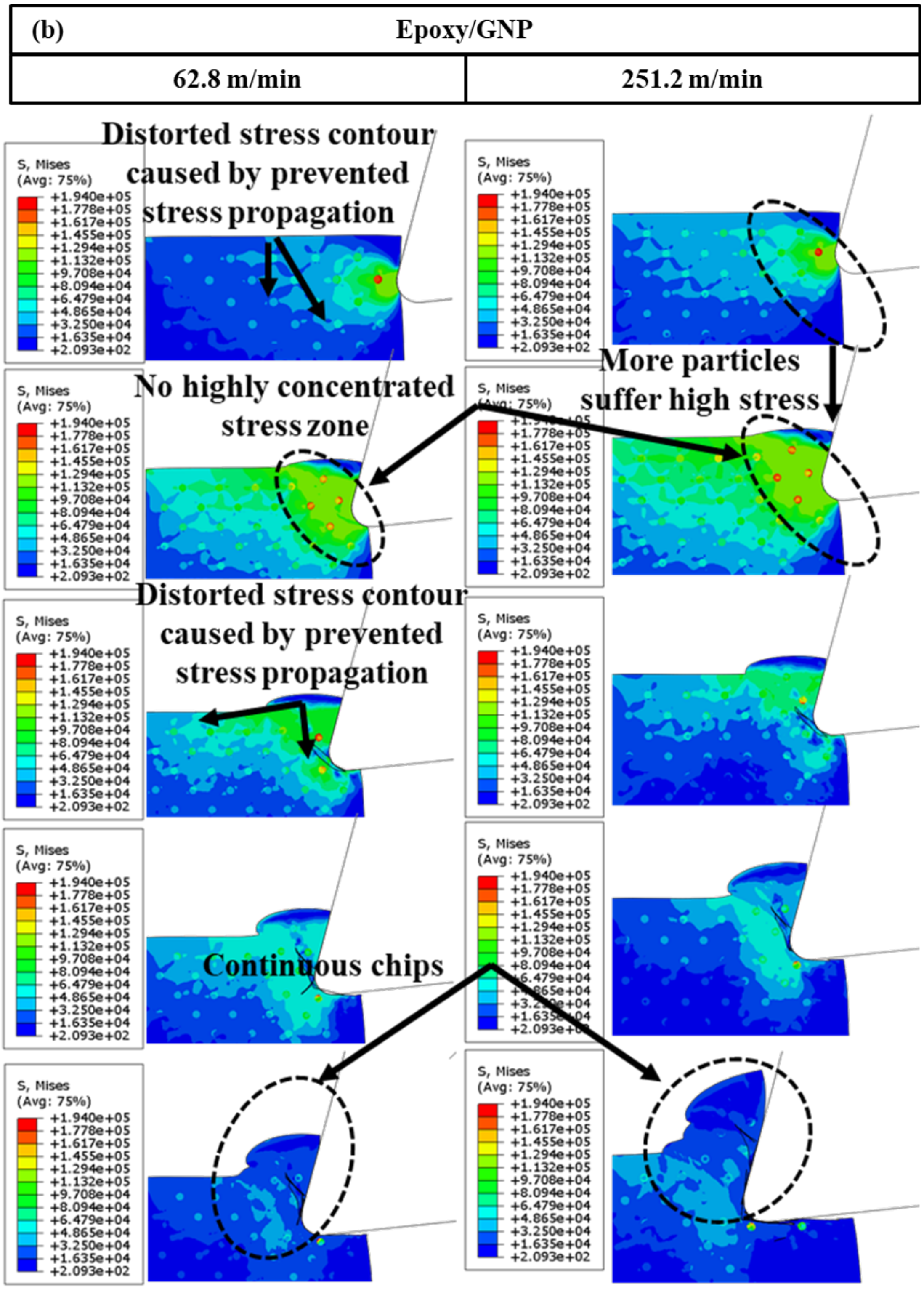

Figure 9. Stress distribution of **(a)** plain epoxy and **(b)** epoxy/GNP with a cutting rate of 2 μm feed per tooth

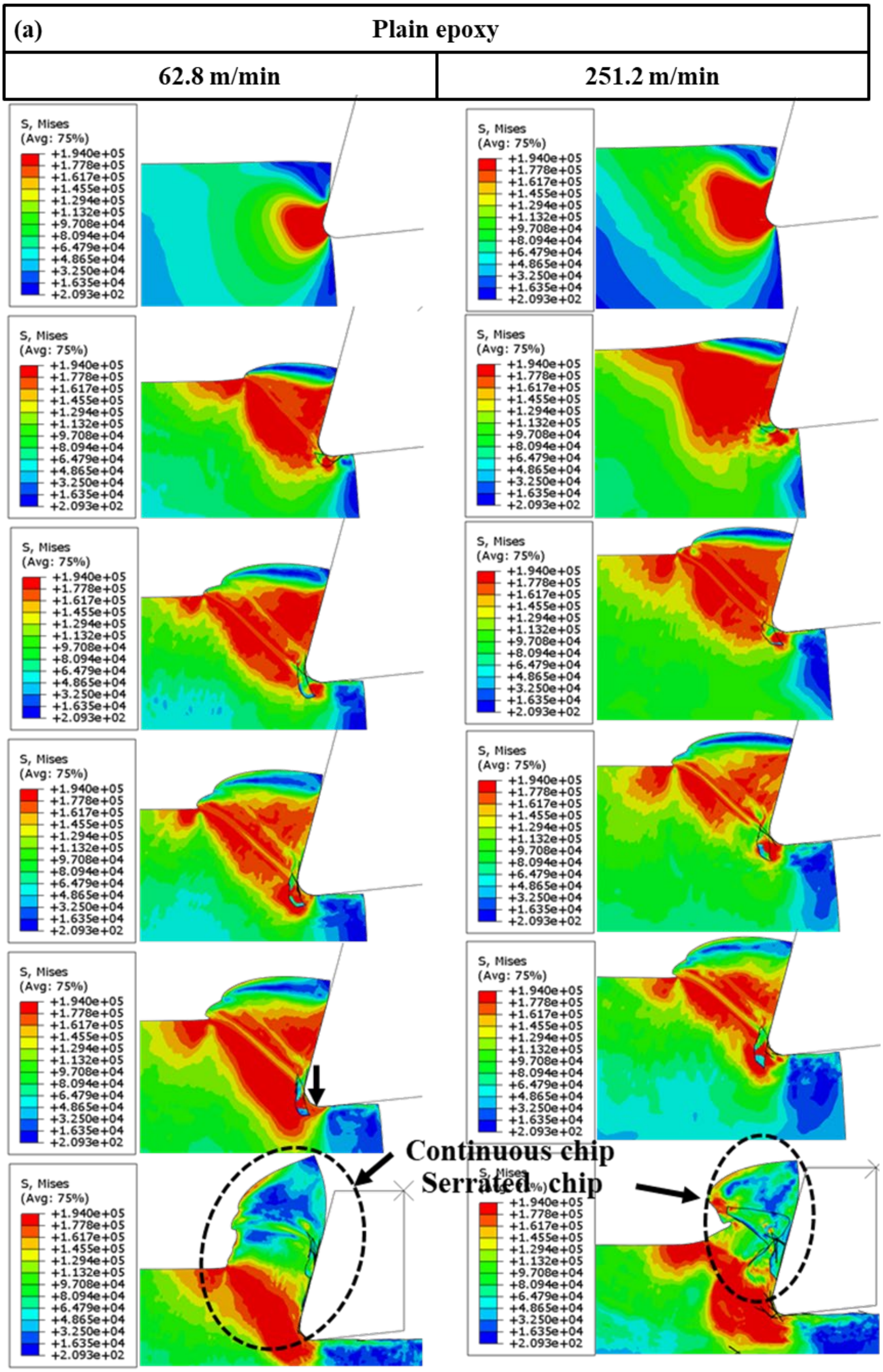
(a)
Plain epoxy
62.8 m/min
251.2 m/min
S, Mises
(Avg: 75%)
+1.940e+05
+1.778e+05
+1.617e+05
+1.455e+05
+1.294e+05
+1.132e+05
+9.708e+04
+8.094e+04
+6.479e+04
+4.865e+04
+3.250e+04
+1.635e+04
+2.093e+02
Continuous chip
Serrated chip

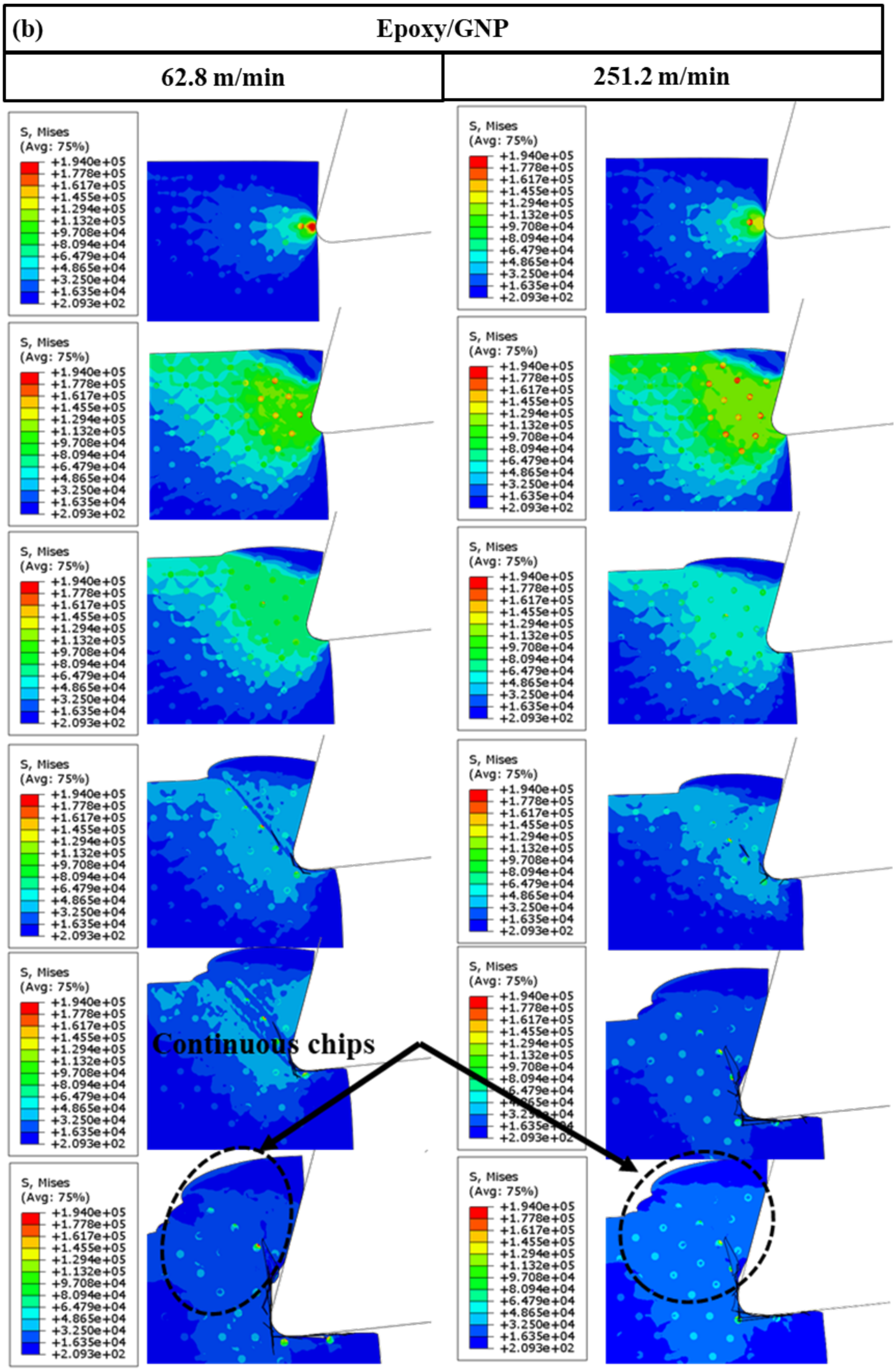

Figure 10. The cutting process of **(a)** plain epoxy and **(b)** epoxy/GNP at 5 μm feed per tooth

5.2 Strain Distribution

Fig. 11 shows the strain distribution in the plain epoxy and epoxy/GNP during the cutting process at 5 μm feed per tooth and a cutting speed of 251.2 m/min. In either cutting, a slender region with severe local deformation called shear band is formed near the tip of the tool in the material and is extended to the free surface of the material. In contrast, the material behind the shear band which is associated with smaller strains slides along the band and form a chip segment. As strong local strain develops at the tool tip, the material in front of the tool tip start to damage and separate from the matrix material, which slides towards the rake face of the tool due to the advance of the tool. Consequently, the formed chip segment is pushed to slide along the rake face and move away from the tool tip. With the continuing advance of the tool, another narrow band then begins to form near the tool when the first band has fully developed, and a new chip segment is forming. This process repeats periodically and a chip consisting of a set of chip segments is formed in the end. Under severe deformation, very high strains may develop in the shear bands and a serrated chip characterized by a saw-tooth profile can be formed.

Although the primary trend of the strain distribution is very similar in the plain epoxy and epoxy/GNP, the two materials still exhibit some differences, as shown in **Fig. 11**. The epoxy/GNP has a smaller shear zone compared to the plain epoxy. Because GNP nanoparticles act as barriers and confine the development of plastic deformation in the matrix, the matrix material experiences less server plastic deformation, making the shear zone in the matrix material smaller than that in the plain epoxy material. During the cutting process, the GNP nanoparticles are not significantly deformed. Therefore, they generate compressive stress on the matrix under the squeezing action of the cutting tool, which causes stress concentration. This phenomenon is consistent with the stress distribution of epoxy/GNP shown in **Fig. 10**.

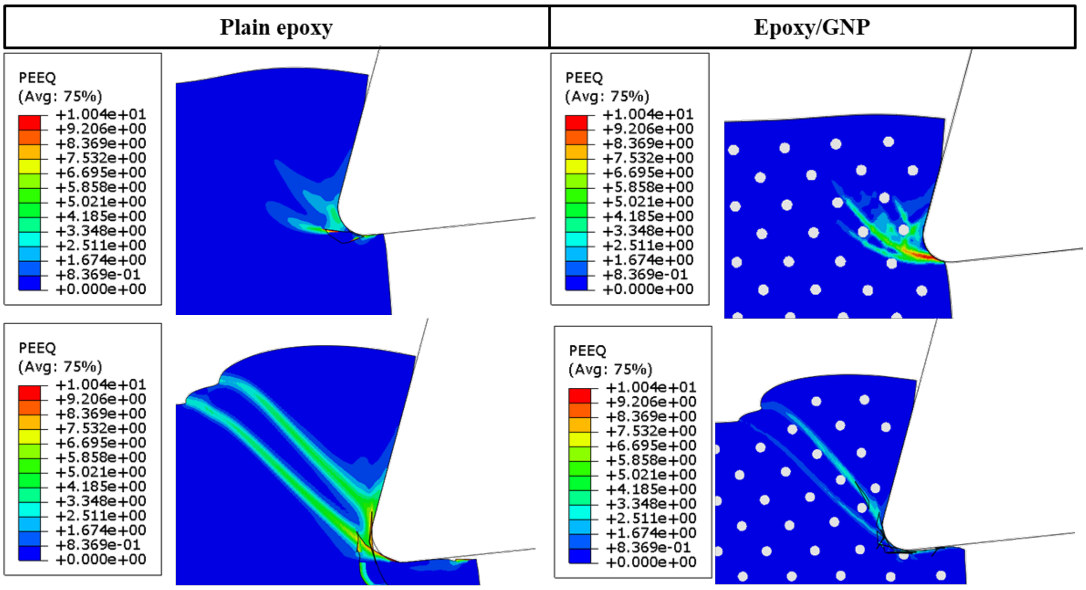

Figure 11. Strain distribution of plain epoxy and epoxy/GNP at the cutting conditions of 5 μm feed per tooth and 251.2 m/min cutting speed

5.3 Chip Deformation

Chips were collected from plain epoxy and epoxy /GNP to verify the chip formation model. **Fig. 12** shows SEM images of chips of plain epoxy and epoxy/GNP formed at 5 μm of feed per tooth and different cutting speeds. The epoxy/GNP nanocomposite has continuous chips at cutting speeds of 62.8 m/min and 251.2 m/min. Plain epoxy presents continuous chips at a cutting speed of 62.8 m/min but tends to form serrated chips at 251.2 m/min. The experimental results agree with the previous simulation results shown in **Fig. 10** closely. The simulation results show that both plain epoxy and epoxy/GNP have developed complete primary shear zones during the cutting process. This indicates that material removal is achieved through shear sliding along the shear bands. The reason for the formation of different types of chips in the two materials under the cutting speed of 251.2m/min is that the nanoparticles bear a lot of stress during cutting, which greatly reduces the shear plastic deformation in the matrix material. Therefore, the chips can still be continuous at this cutting speed. Even though the plain epoxy and epoxy/GNP chips exhibit different chip deformation characteristics at high cutting speeds, the chip deformation mechanism itself is not changed by the presence of GNP particles. Both cutting processes of epoxy/GNP and plain epoxy belong to the chip formation involving a shear plastic slip mechanism.

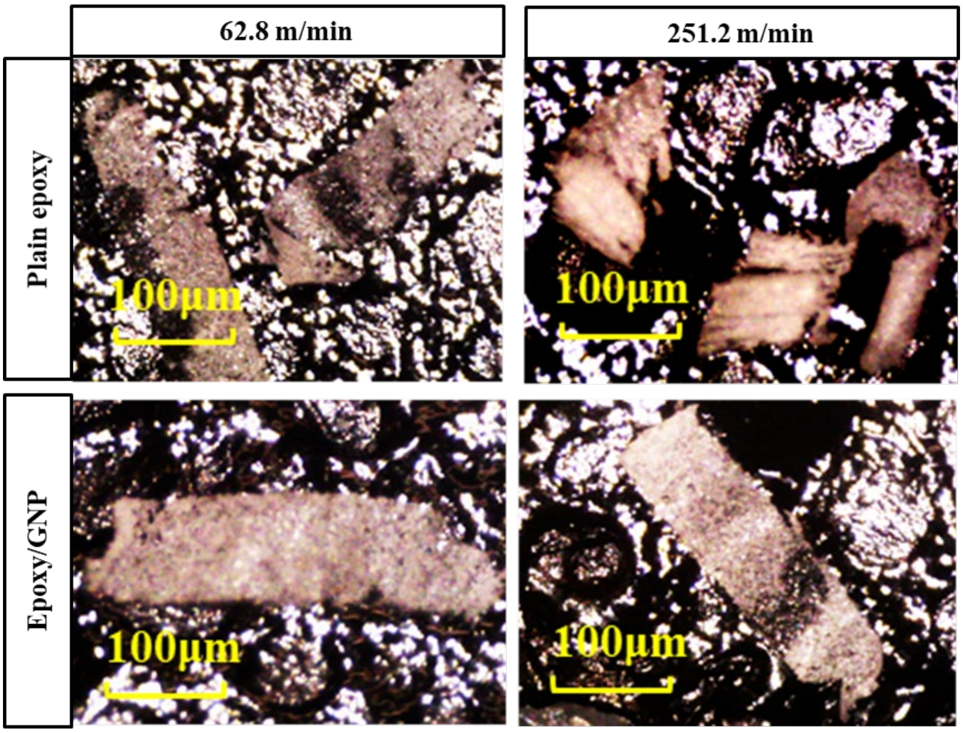

Figure 12. SEM images of chips of plain epoxy and epoxy/GNP at 5 μm of feed per tooth and different cutting speeds

5.4 The Machined Surface and Cutting Force

Fig. 13 shows tool-particle interaction during the cutting process at 2 μm of feed per tooth and the cutting speed of 251.2 m/min. It shows that cavities are formed when the GNP particles are located on the cutting path and the matrix surrounding them is ruptured from the rest of the matrix. The nanoparticles would cause excessive compressive stress on the machined surface, leading to matrix failure or irreversible plastic deformation. Compared with the cutting of the plain epoxy, small cracks appear on the machined surface of epoxy/GNP in the direction of the tool path, which undermines the integrity of the machined surface. The simulation results show that small cavities/cracks can be found in about 40% area of machined surface in the epoxy/GNP, while no cavities/cracks are found on the machined surface in the plain epoxy.

Fig. 13 (d) shows that the nanoparticle is embedded within the machined surface and slides with the cutting tool, resulting in the sliding behaviour of the GNP nanoparticle on the tool rake face and a highly localised contact. During the interaction between the tool and the particles, a cavity is formed when the particles on the cutting path and the immediately surrounding matrix are ruptured from the rest of the matrix. The pressing of nanoparticles into the machined surface will thus cause damage to the matrix or irreversible plastic deformation, resulting in excessive compressive stress. Therefore, it is speculated that epoxy/GNP and plain epoxy have different machined surface morphologies. The nanoparticles located in the cutting path are partially embedded within the newly machined surface, which might be considered as one of the main factors contributing to surface deterioration. **Fig. 14** shows SEM images of the machined surfaces of plain epoxy and epoxy/GNP at 2 μm of feed per tooth and the cutting speed of 251.2 m/min. The machined surface of plain epoxy is flat and smooth, while the surface of the epoxy/GNP presents small cracks.

Fig. 13 (d) also shows that the nanoparticles located along or below the cutting path are pressed into the matrix. These particles act as sharp cutting-edge, leading to increased residual stress or severe plastic deformation on the machined surface. This phenomenon has been widely acknowledged by researchers in both experimental and simulation work [43]. Generally, high contact stress at the tool-particle interface has been recognised as the main cause of tool wear. Fu et al. [43] demonstrated that with the addition of GNP, the tool wear of uncoated micro end tools increases slightly and the rounding of the tool tip as well as relatively smooth abrasive wear can be observed on the flank face. The mobility of the GNP nanoparticles with matrix deformation is a factor contributing to the pattern of smooth abrasive wear. Although GNP particles increase tool wear, the increased wear is relatively slight compared with that caused by other particles, due to the small size of the GNP which results in less kinematic energy during tool-particle interaction [37,38].

Fig. 15 shows the simulation cutting force obtained in the machining of plain epoxy and epoxy/GNP at 2 μm of feed per tooth and 251.2 m/min of cutting speed. Compared with the cutting of plain epoxy, it can be observed that the cutting force obtained in the epoxy/GNP is associated with stronger fluctuations. This can be explained in terms of tool-particle interaction behaviour and the nanoparticles' increased kinetic energy. The simulation cutting force of epoxy/GNP is about 30% higher than plain epoxy. However, the simulated value of the cutting force in the epoxy/GNP of about 2 N/m is lower than that found in the experiment, 3 N/m [43]. The simulation value in the plain epoxy of about 1.5 N/m is also lower than that the experiment value of about 2 N/m [43]. There may be three reasons for this [45]: (1) the Mulliken-Boyce model may have limitations at high-rate loads; (2) the current modelling does not include the effect of adhesion at the chip-tool interface; (3) the strain gradient effect is not considered in this modelling.

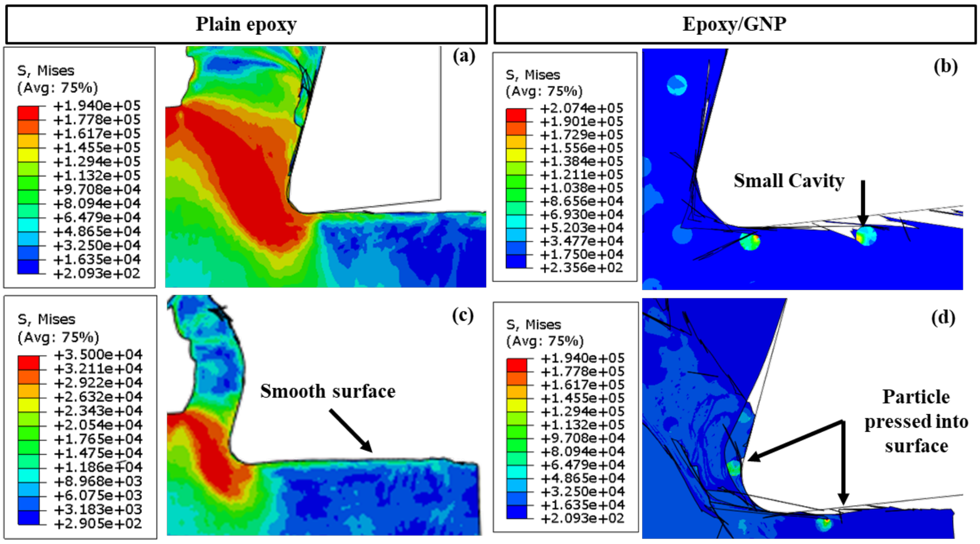

Figure 13. GNP nanoparticles interacting with the cutting tool at 2 μm of feed per tooth and 251.2 m/min of cutting speed

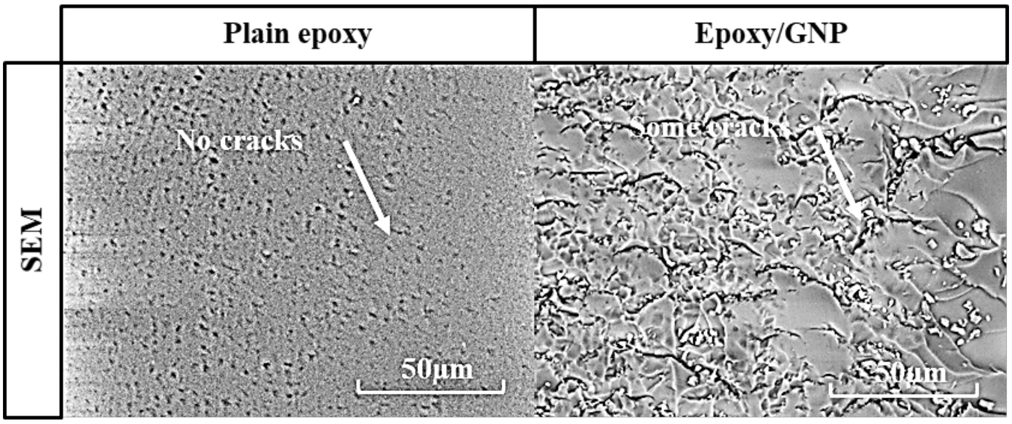

Figure 14. SEM images of the machined surface of plain epoxy and epoxy/GNP at 2 μm of feed per tooth and 251.2m/min of cutting speed

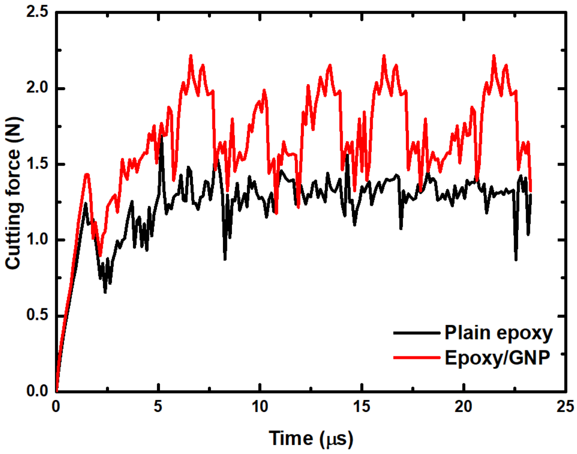

Figure 15. Simulation cutting forces for plain epoxy and epoxy/GNP at 2 μm of feed per tooth and 251.2m/min of cutting speed

6 Conclusion

This study has established a two-dimensional FE model for the cutting of polymer/GNP nanocomposite using a rate-dependent model. The deformation behaviour and cutting characteristics of the materials in terms of chip formation, stress/strain distribution, and surface cracks are studied. This study draws the following conclusions:

- During the cutting process, GNP nanoparticles are subjected to relatively high stress transferred from the matrix material. The GNP nanoparticles can be recognised as the obstacle restricting the extension and progression of plastic strains in the material.
- The cutting force for the epoxy/GNP is about 30% higher than that for the plain epoxy, which is agreement with the experimental results.
- At high cutting speeds, plain epoxy resin and epoxy /GNP produce different chips. The presence of GNP nanoparticles is not sufficient to change the chip deformation mechanism, but it influences the plastic deformation in the chip and hence influences the chip profile. The removal of epoxy resin/GNP and plain epoxy belongs to the shear plastic slip mechanism.
- Compared with the plain epoxy, small cracks are generated on up to 40% of the machined surface of epoxy/GNP, which leads to undesired surface integrity.
- GNP nanoparticles embedded within the machined surface slide along with the cutting tool, resulting in GNPs-tool interactions which can cause tool wear.

Declarations

The authors declare that:

- They have no known competing interests that could have appeared to influence the work reported in this paper;
- All authors give their permission to participate and publish;
- No ethical approval needed for this research;

References

[1] G. A. Silva, “Introduction to nanotechnology and its applications to medicine,” *Surg. Neurol.*, vol. 61, no. 3, pp. 216–220, 2004.

[2] K. Pielichowski and K. Pielichowska, “Polymer Nanocomposites,” in *Handbook of Thermal Analysis and Calorimetry*, vol. 6, 2018, pp. 431–485.

[3] Q. J. Xue and Q. H. Wang, “Wear mechanisms of polyetheretherketone composites filled with various kinds of SiC,” *Wear*, vol. 213, no. 1–2, pp. 54–58, 1997.

[4] W. Qihua, X. Qunji, S. Weichang, and Z. Junyan, “The friction and wear properties of nanometer ZrO2-filled polyetheretherketone,” *J. Appl. Polym. Sci.*, vol. 69, no. 1, 1998.

[5] B. J. Briscoe, Lin Heng Yao, and T. A. Stolarski, “The friction and wear of poly(tetrafluoroethylene)-poly (etheretherketone) composites: An initial appraisal of the optimum composition,” *Wear*, vol. 108, no. 4, pp. 357–374, 1986.

[6] T. Naganuma and Y. Kagawa, “Effect of particle size on the optically transparent nano meter-order glass particle-dispersed epoxy matrix composites,” *Compos. Sci. Technol.*, vol. 62, no. 9, pp. 1187–1189, 2002.

[7] X. Liu, R. E. DeVor, and S. G. Kapoor, “An Analytical Model for the Prediction of Minimum Chip Thickness in Micromachining,” *J. Manuf. Sci. Eng.*, pp. 474-481, 2006.

[8] J. R. Potts, D. R. Dreyer, C. W. Bielawski, and R. S. Ruoff, “Graphene-based polymer nanocomposites,” *Polymer (Guildf).*, vol. 52, no. 1, pp. 5-25, 2011.

[9] H. Kim, A. A. Abdala, and C. W. MacOsko, “Graphene/polymer nanocomposites,” *Macromolecules*, vol. 43, no. 16. pp. 6515–6530, 2010.

[10] A. a. Aly, “Friction and Wear of Polymer Composites Filled by Nano-Particles: A Review,” *World J. Nano Sci. Eng.*, vol. 02, no. 01, pp. 32–39, 2012.

[11] M. A. Rafiee, J. Rafiee, Z. Z. Yu, and N. Koratkar, “Buckling resistant graphene nanocomposites,” *Appl. Phys. Lett.*, vol. 95, no. 22, pp.223103, 2009.

[12] Y. Zhu *et al.*, “Graphene and graphene oxide: Synthesis, properties, and applications,” *Adv. Mater.*, vol. 22, no. 35, pp. 3906-3924, 2010.

[13] B. Wetzel, F. Haupert, K. Friedrich, M. Q. Zhang, and M. Z. Rong, “Impact and wear resistance of polymer nanocomposites at low filler content,” *Polym. Eng. Sci.*, vol. 42,

no. 9, pp. 1919–1927, 2002.

[14] K. Friedrich and S. Fakirov, *Polymer composites: from nano-to-macro-scale.*, Springer Science & Business Media, 2005.

[15] J. Zhao *et al.*, “Facile preparation of one-dimensional wrapping structure: Graphene nanoscroll-wrapped of Fe3O4 nanoparticles and its application for lithium-ion battery,” *ACS Appl. Mater. Interfaces*, vol. 6, no. 12, pp. 9890-9896, 2014.

[16] M. A. Rafiee *et al.*, “Fracture and fatigue in graphene nanocomposites,” *Small*, vol. 6, no. 2, pp. 179–183, 2010.

[17] E. Cerda and L. Mahadevan, “Geometry and Physics of Wrinkling,” *Phys. Rev. Lett.*, vol. 90, no. 7, pp. 074302, 2003.

[18] K. Matan, R. B. Williams, T. A. Witten, and S. R. Nagel, “Crumpling a thin sheet,” *Phys. Rev. Lett.*, vol. 88, pp. 7-10, 2002.

[19] R. Atif, I. Shyha, and F. Inam, “Modeling and experimentation of multi-layered nanostructured graphene-epoxy nanocomposites for enhanced thermal and mechanical properties,” *J. Compos. Mater.*, vol. 51, no. 2, pp. 209-220, 2017.

[20] F. Sun, U. Wiklund, F. Avilés, and E. K. Gamstedt, “Assessing local yield stress and fracture toughness of carbon nanotube poly(methyl methacrylate) composite by nanosectioning,” *Compos. Sci. Technol.*, vol. 153, pp. 95-102, 2017.

[21] M. López-Suárez, F. Torres, N. Mestres, R. Rurali, and G. Abadal, “Fabrication of highly regular suspended graphene nanoribbons through a one-step electron beam lithography process,” *Microelectron. Eng.*, vol. 129, pp. 81-85, 2014.

[22] M. Y. Han, B. Özyilmaz, Y. Zhang, and P. Kim, “Energy band-gap engineering of graphene nanoribbons,” *Phys. Rev. Lett.*, vol. 98, no. 20, pp. 206805, 2007.

[23] J. Samuel, R. E. DeVor, S. G. Kapoor, and K. J. Hsia, “Experimental Investigation of the Machinability of Polycarbonate Reinforced With Multiwalled Carbon Nanotubes,” *J. Manuf. Sci. Eng.*, vol. 128, no. 2, p. 465, 2006.

[24] X. Teng, D. Huo, W. Chen, E. Wong, L. Zheng, and I. Shyha, “Finite element modelling on cutting mechanism of nano Mg/SiC metal matrix composites considering cutting edge radius,” *J. Manuf. Process.*, vol. 32, pp. 116–126, 2018.

[25] R. Atif, J. Wei, I. Shyha, and F. Inam, "Use of morphological features of carbonaceous materials for improved mechanical properties of epoxy nanocomposites," *RSC Adv.*, vol. 6, no. 2, pp. 1351-1359, 2016.

[26] J. Wei, "Graphene in epoxy system: Dispersion, preparation and reinforcement effect." Ph.D. thesis (unpubl.), Northumbria University, 2017.

[27] B. Wetzel, F. Haupert, and M. Q. Zhang, "Epoxy nanocomposites with high mechanical and tribological performance," *Compos. Sci. Technol.*, vol. 63, no. 14, pp. 2055–2067, 2003.

[28] M. Saharudin, "Mechanical properties of polyester nano-composites exposed to liquid media." Ph.D. thesis (unpubl.), Northumbria University, 2017.

[29] X. Lai, H. Li, C. Li, Z. Lin, and J. Ni, "Modelling and analysis of micro scale milling considering size effect, micro cutter edge radius and minimum chip thickness," *Int. J. Mach. Tools Manuf.*, vol. 48, no. 1, pp.1-14, 2008.

[30] E. M. Arruda and M. C. Boyce, "Evolution of plastic anisotropy in amorphous polymers during finite straining," *Int. J. Plast.*, vol. 9, no. 6, pp. 697–720, 1993.

[31] A. D. Mulliken and M. C. Boyce, "Mechanics of the rate-dependent elastic-plastic deformation of glassy polymers from low to high strain rates," *Int. J. Solids Struct.*, vol. 43, no. 5, pp. 1331–1356, 2006.

[32] J. S. Bergström and M. C. Boyce, "Large strain time-dependent behavior of filled elastomers," *Mech. Mater.*, vol. 32, no. 11, pp. 627-644, 2000.

[33] M. C. Boyce, D. M. Parks, and A. S. Argon, "Large inelastic deformation of glassy polymers, part II: numerical simulation of hydrostatic extrusion," *Mech. Mater.*, vol. 7, pp. 35–47, 1988.

[34] A. G. Varghese and R. C. Batra, "Constitutive equations for thermomechanical deformations of glassy polymers," *Int. J. Solids Struct.*, vol. 46, no. 22-23, pp. 4079-4094, 2009.

[35] X. Teng, D. Huo, W. Chen, E. Wong, L. Zheng, and I. Shyha, "Finite element modelling on cutting mechanism of nano Mg/SiC metal matrix composites considering cutting edge radius," *J. Manuf. Process.*, vol. 32, pp. 116–126, 2018.

[36] J. R. Foley, J.L. Jordan, and C.R. Siviour, , “Constitutive modeling of epoxy using the Mulliken-Boyce model for glassy polymers,”CAMBRIDGE UNIV (UNITED KINGDOM) CAVENDISH LAB, 2008.

[37] M. A. Rafiee, J. Rafiee, Z. Wang, H. Song, Z. Z. Yu, and N. Koratkar, “Enhanced mechanical properties of nanocomposites at low graphene content,” *ACS Nano*, vol. 3, no. 12, pp. 3884–3890, 2009.

[38] G. Dai and L. Mishnaevsky, “Fatigue of multiscale composites with secondary nanoplatelet reinforcement: 3D computational analysis,” *Compos. Sci. Technol.*, vol. 91, pp. 71-81, 2014.

[39] J. Cho, J. Y. Chen, and I. M. Daniel, “Mechanical enhancement of carbon fiber/epoxy composites by graphite nanoplatelet reinforcement,” *Scr. Mater.*, vol. 56, no. 8, pp. 685-688, 2007.

[40] C. Lee, X. Wei, J. W. Kysar, and J. Hone, “Measurement of the elastic properties and intrinsic strength of monolayer graphene,” *Science (80-.).*, vol. 321, no. 5887, pp. 385-388, 2008.

[41] P. Zhang *et al.*, “Fracture toughness of graphene,” *Nat. Commun.*, vol. 5, no. 1, pp. 1-7, 2014.

[42] D. G. Papageorgiou, Z. Li, M. Liu, I. A. Kinloch, and R. J. Young, “Mechanisms of mechanical reinforcement by graphene and carbon nanotubes in polymer nanocomposites,” *Nanoscale.*, vol. 12, no. 4, pp. 2228-2267, 2020.

[43] G. Fu, D. Huo, I. Shyha, K. Pancholi, and B. Alzahrani, “Experimental investigation on micromachining of epoxy/graphene nano platelet nanocomposites,” *Int. J. Adv. Manuf. Technol.*, vol. 107, no. 7, pp. 3169-3183, 2020.

[44] X. Teng, D. Huo, I. Shyha, W. Chen, and E. Wong, “An experimental study on tool wear behaviour in micro milling of nano Mg/Ti metal matrix composites,” *Int. J. Adv. Manuf. Technol.*, vol. 96, no. 5, pp. 2127-2140, 2018.

[45] F. Sun and E. K. Gamstedt, “Experimental and numerical investigation on shear banding during nanomachining of an amorphous glassy polymer,” *Int. J. Mech. Sci.*, vol. 151, pp. 13-21, 2019.